Title

A study of silver acetate under extreme conditions

Journal

Physical Chemistry Chemical Physics, 28(11)

ISSN

1463-9076

Authors

Bhandari, Govinda
Kunz, Martin
Pravica, Michael

Publication Date

2026-03-18

DOI

10.1039/d5cp04790k

View Article Online
DOI: 10.1039/D5CP04790K

Studies of Silver Acetate at Extreme Conditions

Govinda Bhandari [a], Martin Kunz [b], Michael Pravica [a] *

[a] Department of Physics and Astronomy, University of Nevada, Las Vegas, Las Vegas, NV 89154, USA

[b] Lawrence Berkeley National Laboratory, Berkeley, CA 94720, USA

Corresponding author: Michael Pravica * Email: michael.pravica@unlv.edu

Abstract

With an aim of exploring further chemical systems that may metallize when irradiated with hard X-rays, we studied select silver acetate ($AgC_2H_3O_2$). X-ray–induced decomposition of silver acetate under ambient and high-pressures conditions was observed in a diamond anvil cell (DAC), leading to the formation of metallic nanograins of silver at ambient and 1.65 GPa. At 4 GPa, no decomposition was observed. The Avrami kinetics equation also provides information about novel structural formation at ambient and 1.65 GPa pressure. By modeling XRD data, the size of the formation of silver nano crystallite size at 1.65 GPa pressure was found to grow to 5.14 ± 0.02 nm upon X-ray irradiation when the data are fitted with the Boltzmann sigmoidal function. Time-resolved X-ray diffraction (XRD) reveals pressure-dependent kinetics, demonstrating that coupling pressure with irradiation enables controlled photochemical pathways in this model system. Concurrent with previous studies, the application of high pressure (HP) can be considered as a means of controlling X-ray synthetic photochemistry.

Keywords: X-rays; High pressure; Diamond anvil cell; Silver acetate; XRD; Photochemistry

View Article Online
DOI: 10.1039/D5CP04790K

1. Introduction

By harnessing highly energetic, focused and penetrating hard x-rays (>7keV) with no addition of heat or catalysts, we have demonstrated the ability to synthesize novel materials[1], novel structures of known materials[2], and otherwise perform highly controllable chemistry at extreme and ambient conditions[3]. As part of our efforts to expand and demonstrate the utility of useful hard x-ray photochemistry, we have recently demonstrated x-ray induced metallization of salts by irradiating tin oxalate with x-rays[4]. In an effort to better understand the nature of x-ray-initiated electron transfer leading toward metallization, we sought to examine the effect of irradiating silver-containing salts. High-pressure studies of metals and salts using X-ray diffraction (XRD) provide a powerful approach to control reaction kinetics, phase stability, and nanostructure formation. In this context, silver salts are of particular interest because they serve as efficient precursors for generating metallic silver. X-rays have long been used to probe electronic structure, bonding, and decomposition processes[2]. More recently, X-ray–induced damage in solids has been shown to be tunable and even exploitable as a synthetic tool[4]. Prior studies indicate that X-rays can break molecular bonds through ultrafast electronic relaxation, with outcomes governed by chemical environment, photon flux, intermolecular spacing, and X-ray energy all of which can be modulated by applied pressure[5]. Experiments on simple salts and oxalates have demonstrated that modest compression can accelerate X-ray-driven reactions, enabling the formation of novel products[6,7]. Electronic relaxation dynamics following X-ray excitation depends strongly on local chemistry, initial charge state, intermolecular distances, and photon energy[8–10]. In particular, high pressure (HP) is a

View Article Online
DOI: 10.1039/D5CP04790K

key parameter for tuning intermolecular distances, reaction manifolds and activation energies[7,11–13].

Nanomaterial metals have attracted substantial attention to applications spanning nanomedicine, optoelectronics, and catalysis[14,15]. Metal nanoparticles exhibit unique optical, electronic, magnetic, and mechanical properties that make them a major research focus. Among these, silver nanoparticles show strong promise for optics, molecular sensing, catalysis, and healthcare [16–19]. Metal formation and refinement can be achieved through multiple routes, such as chemical decomposition, reduction reactions, hydrothermal and solvothermal synthesis, chemical vapor deposition, and gas-phase techniques[20–23]. Additional physical methods (e.g., laser ablation, evaporation–condensation, and sputtering) and biological approaches using plant extracts, bacteria, fungi, or algae have also been reported for silver nanoparticle synthesis[24–27]. Silver is technologically important due to its exceptional electrical and optical properties[14,15,28]. It possesses very high electrical conductivity and low contact resistance, enabling widespread use in electronics, reliable electrical contacts, solder and brazing alloys, and printed conductors[29]. Owing to its excellent reflectivity, silver is extensively employed in mirrors and reflective coatings[30]. In clean-energy technologies, silver is essential in photovoltaic (PV) cells, where front and back side silver pastes collect and conduct current[31]. It is also integral to emerging transparent electrodes based on silver nanowires and silver inks[32]. Beyond electronics and energy, silver's strong antimicrobial properties motivate the use of thin silver coatings in medical devices such as catheters and wound dressings[33]. Industrially, silver serves as a key catalyst in the production of ethylene oxide from ethylene[34]. These broad applications highlight the need for tunable synthetic

View Article Online
DOI: 10.1039/D5CP04790K

pathways to produce nanostructured silver with controlled morphology and crystallinity. The thermally decomposed silver acetate ($AgC_2H_3O_2$) is widely used as a precursor for synthesizing diverse silver nanostructures including nanowires, nanorods, plasmonic particles, and catalytic nanoparticles with demonstrated utility in electronic and catalytic systems[35]. Motivated by these insights, we investigated the combined effects of high pressure, monochromatic X-ray irradiation, and *in situ* XRD on the controlled decomposition of silver acetate and the possible formation of metallic silver.

Previous work has shown that decomposition efficiency and transformation yield are enhanced when the incident X-ray energy is tuned slightly above the K-edge of the target cation[4]. For example, Cadmium oxalate's experiment was performed at 27 keV, slightly above the Cd K edge 26.714 keV. Cadmium carbonate ($CdCO_3$) was produced via X-ray-induced decomposition of cadmium oxalate (CdC_2O_4) at pressures between 0.5 and 1 GPa[8]. Likewise, cesium oxalate monohydrate experiment was carried out at 36 keV, near to the K-edge of cesium 35.987 keV. Cesium superoxide (CsO_2) was formed by irradiating cesium oxalate monohydrate ($Cs_2C_2O_4 \cdot H_2O$) at 0.3, 0.8, and 2.4 GPa[6]. Additional experiments on strontium and barium nitrates revealed the formation of NO_2 and O_2 gases near 0.5 GPa[36]. These studies collectively underscore the strong coupling between pressure, intermolecular spacing, and X-ray-driven reaction dynamics, and they motivate the exploration of silver acetate as a pressure dependent X-ray responsive precursor for generating metallic silver. In this study, we sought to identify controlling parameters, and better understand how pressure tuned, X-ray related pathways may expand the synthesis toolkit for silver nanomaterials.

View Article Online
DOI: 10.1039/D5CP04790K

2. Experimental Methods

Symmetric style diamond anvil cells (DAC's) were used for sample pressurization. The DAC diamonds each had a culet face of 300 μm in diameter. Stainless steel gaskets initially of 250 μm thickness were pre-indented to ~ 60 μm in thickness and then drilled to 120 μm using an electric discharge machine (EDM). Powdered silver acetate ($AgC_2H_3O_2$) was loaded into each DAC with a ruby sphere for pressure measurements. No pressure transmitting medium was used in either sample.

Monochromatic angle-dispersive powder XRD measurements were performed at beamline 12.2.2 at the Advanced Light Source of Lawrence Berkeley National Laboratory at room temperature. A tunable Si (111) double-crystal monochromator was used to filter 'white' X-ray radiation and deliver X-rays of fixed but settable energies. The incident X-ray energy was 25.8 keV (λ = 0.4805 Å), with a relative energy bandwidth ($\Delta E/E$) of approximately 10^{-4}. The photon flux at the sample position was on the order of 10^{11} photons/s, as specified by the beamline characteristics. The beam was focused on a circular spot with a diameter of approximately 10 μm at the sample position using Kirkpatrick-Baez mirrors. XRD patterns were collected using a Dectris Pilatus3 S 1M hybrid photon counting detector (pixel size 0.172 mm, 1-mm Si sensor), with diffraction patterns collected for 60 secs every 5 minutes. All measurements were carried out at room temperature. Pressure was measured using an offline ruby fluorescence spectrometer located at Beamline 12.2.2. The pressure was determined by monitoring the shift of the R1 emission line from a small ruby chip loaded inside the diamond anvil cell. The observed fluorescence shift was converted to

View Article Online
DOI: 10.1039/D5CP04790K

pressure using the standard ruby calibration, and pressure values were calculated using a ruby fluorescence pressure calculator[37]. The instrumental parameters (sample to detector distance, tilt of detector plane) were calibrated using a LaB_6 standard (NIST Standard Reference Material 660). The Kohzu monochromator was calibrated via the absorption edge of Mo (20000eV). The energy accuracy of the calibrated monochromator is better than 2 eV. All diffraction images were integrated by Dioptas software[38] to produce intensity versus 2θ patterns.

3. Results and Discussion

Powdered silver acetate samples were loaded into a DAC and examined over a pressure range of 0–4 GPa. Figure 1 shows the XRD pattern of silver acetate measured at ambient and high pressure (1.65 and 4.0 GPa) after 5 minutes of X-ray irradiation. As the pressure increases the XRD patterns shift toward higher 2θ values. The vertical magenta marks indicate the reflections of the previously reported triclinic silver acetate structure (space group $P\bar{1}$, Z =2) and the fitted lattice parameters are a =5.5810(11) Å, b = 9.960(2) Å, c = 21.587(4) Å, α = 89.10(3)◦, β = 97.40(3)◦, γ = 97.26(3)◦[39]. The vertical bars in the figure are the reported crystal structure of silver acetate which matches our experimental ambient data at initial (5 minutes) X-ray irradiation. Additionally, samples further exposure of X-ray for 25 minutes most of the original peaks start to decrease and new peaks form indicating the formation of metallic silver. The sample was pressurized to 1.65 GPa as measured offline via a ruby fluorometer. Subsequently, it was translated laterally by ~50

View Article Online
DOI: 10.1039/D5CP04790K

μm to access a fresh, unirradiated region of the sample. As the pressure increases to 1.65 GPa, several sharp peaks decrease, and new peaks are formed into broader features. When silver acetate pressurized, distortion of the electron density distribution under X-ray becomes more prominent. The pressure then increased to 4.0 GPa after moving to a new region of unirradiated sample, and XRD patterns were recorded. The absence of any new peaks and the persistence of the original peaks in all XRD patterns indicate that silver acetate does not undergo a phase transition up to 4.0 GPa.

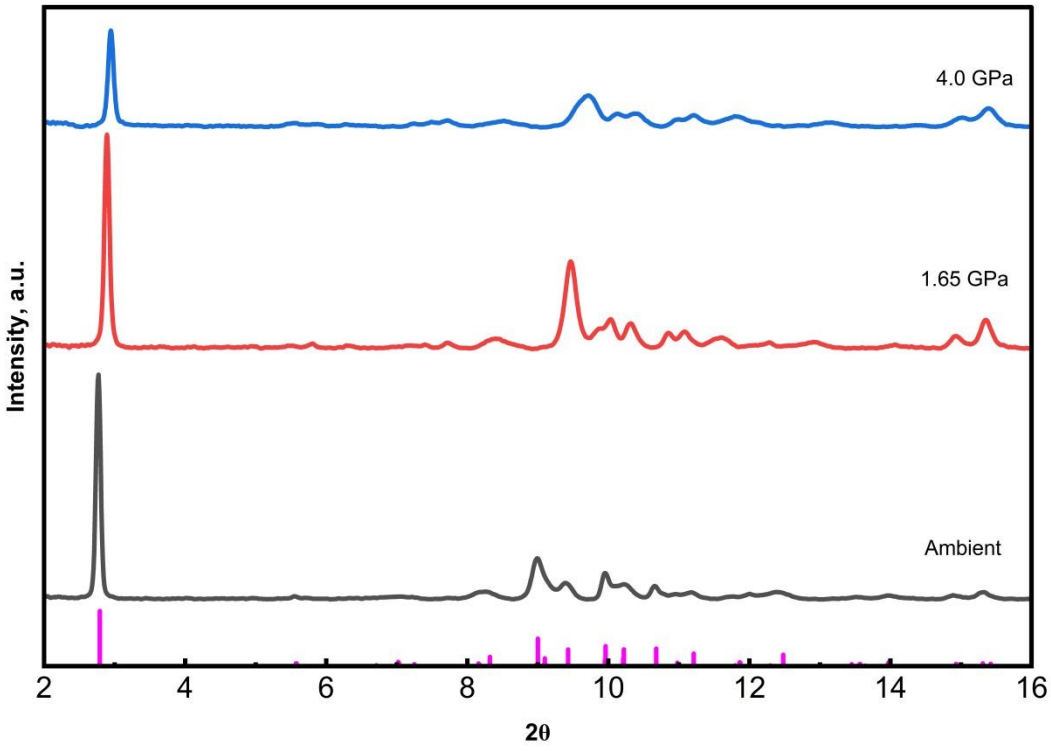

Figure 1: XRD patterns of silver acetate ($AgC_2H_3O_2$) after 5 minutes X-ray irradiation times at 25.8keV. The vertical magenta bars indicate the peaks positions of the previously reported silver acetate triclinic crystal structure[39].

View Article Online
DOI: 10.1039/D5CP04790K

Cell parameters were extracted by means of Le-Bail refinement using a pseudo-Voight profile function in GSAS-II software[40] and also peak-position based unit-cell refinement implemented in Python are reported in Table 1. The X-ray energy has selected 25.8keV which is slightly above the cation's K-edge 25.5keV, this energy was used for all irradiations of experiments[41]. As the pressure increased, the silver acetate Bragg peaks shifted systematically toward higher 2θ angles, consistent with a decrease in d spacing due to elastic lattice compression. The continuous volume compression shows no evidence of pressure induced phase transformation and thus the formation of silver in our experiment must be due to X-ray induced photoreduction rather than pressure driven decomposition.

Table 1: Unit-cell parameters for silver acetate ($P\bar{1}$, Z = 2). At ambient, 1.65 GPa and 4.0 GPa with refinement.

Pressure (GPa)	**a (Å)**	**b (Å)**	**c (Å)**	**α (°)**	**β (°)**	**γ (°)**	**Volume (Å³)**
Ambient	5.593 (12)	10.018 (90)	21.734 (80)	90.040 (60)	97.466 (14)	97.313 (30)	1197.64 (17)
1.65	5.575 (11)	9.6388 (90)	21.830 (91)	89.990 (70)	96.791 (21)	99.154 (29)	1149.66 (19)
4.0	5.495 (37)	9.8472 (51)	21.292 (29)	88.856 (57)	96.588 (88)	97.144 (46)	1135.60 (88)

View Article Online
DOI: 10.1039/D5CP04790K

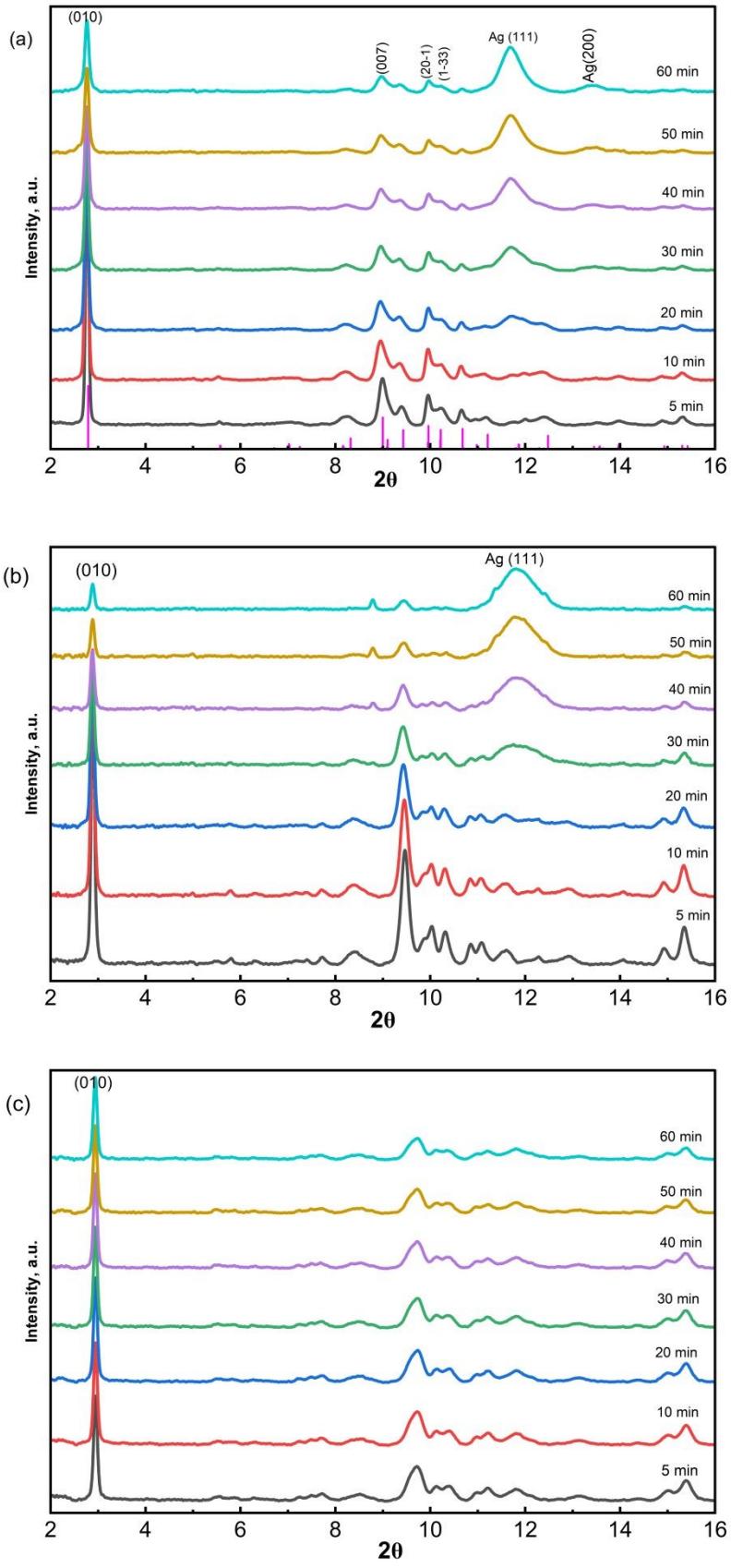

View Article Online
DOI: 10.1039/D5CP04790K

Figure 2: XRD patteren of silver acetate at 1 hour times of X-ray irradation: (a) at ambient pressure (b) silver acetate at 1.65 GPa (c) silver acetate at 4.0 GPa. The magenta bar indicates the previously reported for silver acetate.

In Figure 2 the XRD patterns of silver acetate at ambient conditions and under the experimental selected HP points (1.65 and 4.0 GPa) after irradiation up to 1 hour. As shown in Figure 2 similar trends in peak evolution are observed under both ambient and 1.65 GPa pressures during irradiation of X-rays as a function of time.

In Figure 3 the initial pattern after 5 minutes of X-ray exposure matches the previously reported triclinic crystal structure of silver acetate (space group P $\bar{1}$). The vertical magenta bars indicate the reference reflections for silver acetate. During X-ray irradiation for 1 hour at ambient conditions, new peaks corresponding to d-spacings of 2.36 Å and 2.04 Å correspond to diffraction angles of 2θ equals to 11.69° and 13.52° appear and grow, which are consistent with silver acetate. With continued irradiation, the sample showed signs of partial decomposition, producing metallic silver and other unknown products. Until 25 mins of X-ray irradiation, the XRD peak positions did not change, and no new peaks position were observed. This demonstrates that there is no structural transformation. After 25 minutes of X-ray irradiation, we observe the appearance of new peaks, indicating the onset of a structural transformation.

View Article Online
DOI: 10.1039/D5CP04790K

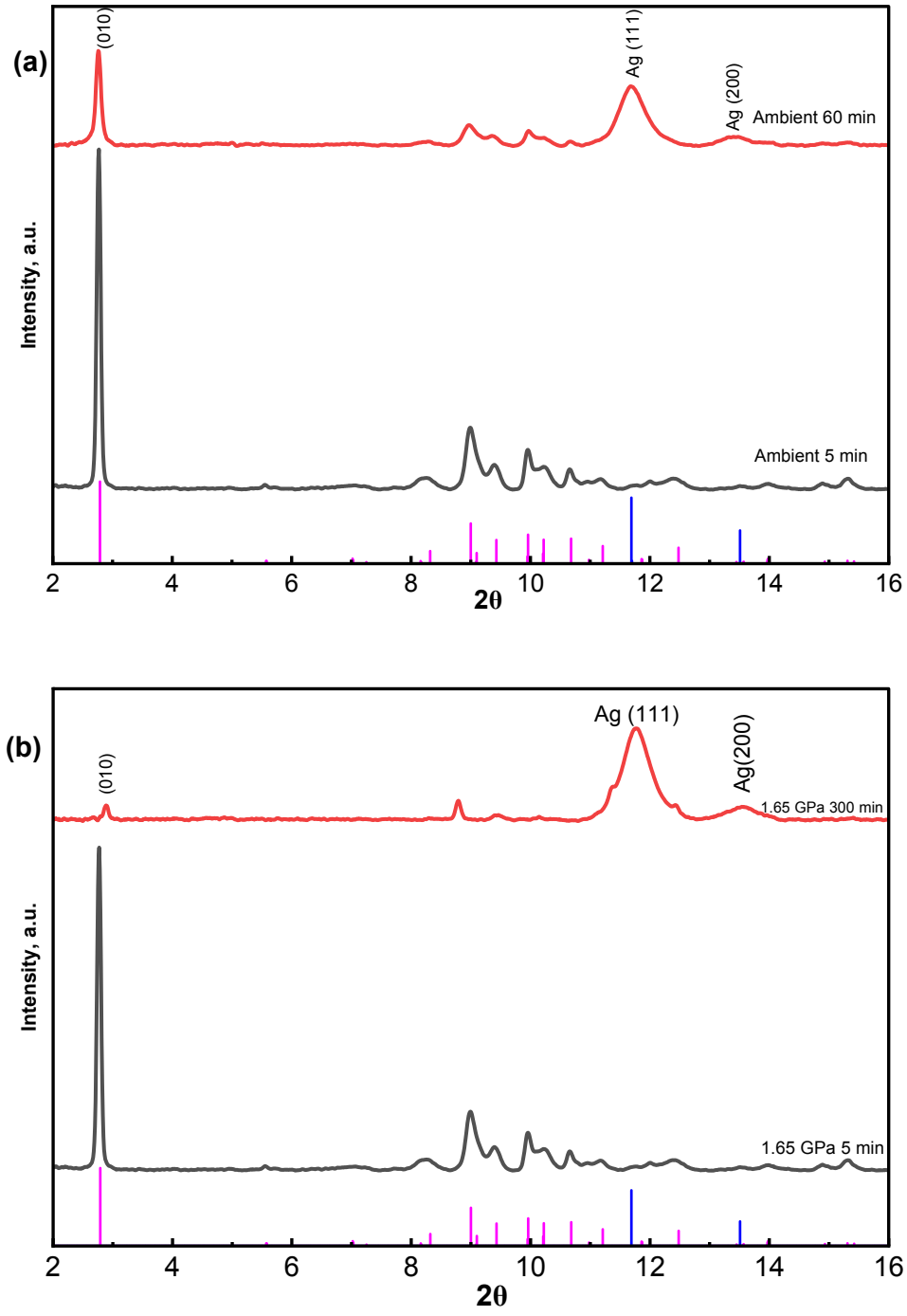

Figure 3: (a). XRD patterns of silver acetate collected at ambient pressure (initial) and 60 minutes of X-ray irradiation. (b). XRD patterns of silver acetate collected at high pressure (initially) and 300 minutes of X-ray irradiation at 1.65 GPa. The vertical magenta bars

View Article Online
DOI: 10.1039/D5CP04790K

correspond to the previously reported triclinic crystal structure of silver acetate, while the vertical blue bars represent the cubic crystal structure of FCC metallic silver.

The final XRD pattern showed new peaks corresponding to the (111), and (200) reflections of metallic Ag (at d-spacings of 2.36 Å and 2.04 Å correspond to diffraction angles of 2θ equals to 11.69° and 13.52°). The positions of the first two peaks matched well with those of cubic metallic Ag, which crystallizes in the Fm–3m space group with lattice parameters $a = b = c$ =4.5643Å and $\alpha = \beta = \gamma = 90\circ$. These reference peak positions, shown as blue vertical bars in (Figure 5)[42,43], were taken from the ICSD database file. The two narrow peaks observed adjacent to the broad Ag reflection are likely attributed to isolated crystallites that are favorably oriented with respect to the incident X-ray beam, thus deviating from poly-cyrstallinity[44]. Moreover, the final XRD pattern retains several peaks from the initial spectrum, indicating that some silver acetate remained undecomposed after irradiation. From this we conclude it is evident that the final product is a mixture of the silver acetate, silver and other unknown products, similar to previously reported findings of X-ray decomposition[4,8]. It should be noted that with increasing pressure and extended irradiation times greater than 10 hours, silver acetate completely decomposed into metallic silver, as evidenced in Figure 4.

View Article Online
DOI: 10.1039/D5CP04790K

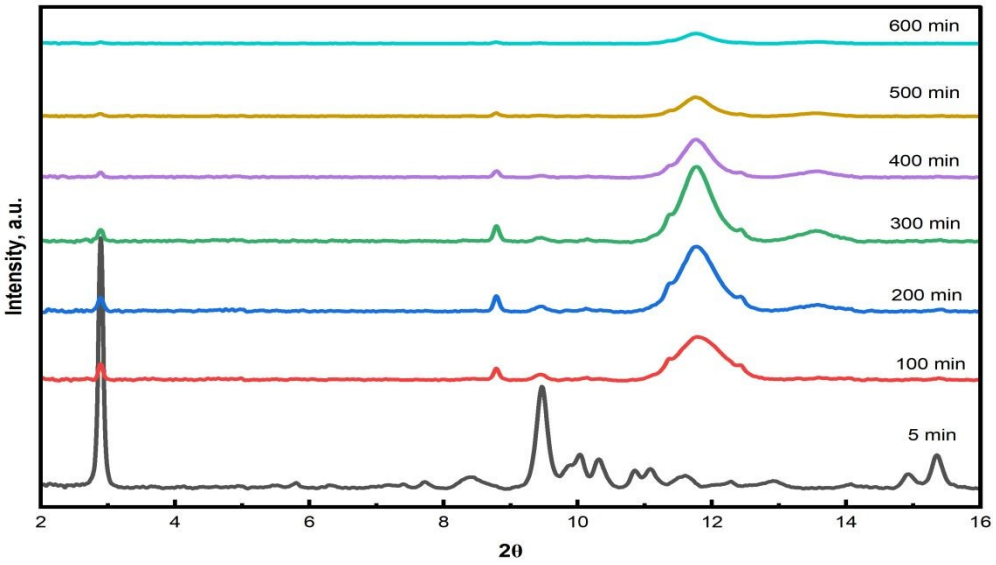

Figure 4: XRD pattern of silver acetate at 1.65 GPa for 10 hours X-ray irradiation.

We compared silver acetate at ambient pressure and at 1.65 GPa by measuring the transformation yield (TY) over X-ray irradiation time. Based on the TY formula, we tracked the rise of silver peaks as a function of X-ray irradiation time. The timing of irradiation and growth were different at the two pressures, suggesting a pressure-dependent transformation kinetics.

$$TY(t) = \frac{A(t)}{A(t_0)} \qquad 1.$$

Here, A(t) is the integrated area of the XRD patterns obtained after several times, irradiation of X-ray and $A(t_0)$ is the integrated area at initial time of irradiation. In the kinetic analysis, the term "integrated area" refers to the integrated intensity of specific diffraction reflections of XRD pattern. The decomposition of silver acetate was quantified using the integrated intensity of its (010) reflection ($2\theta \approx 2.3° – 3.0°$), while the growth of

View Article Online
DOI: 10.1039/D5CP04790K

metallic silver was monitored using the integrated intensity of the Ag (111) reflection (2θ ≈ 11.0° – 12.7°).

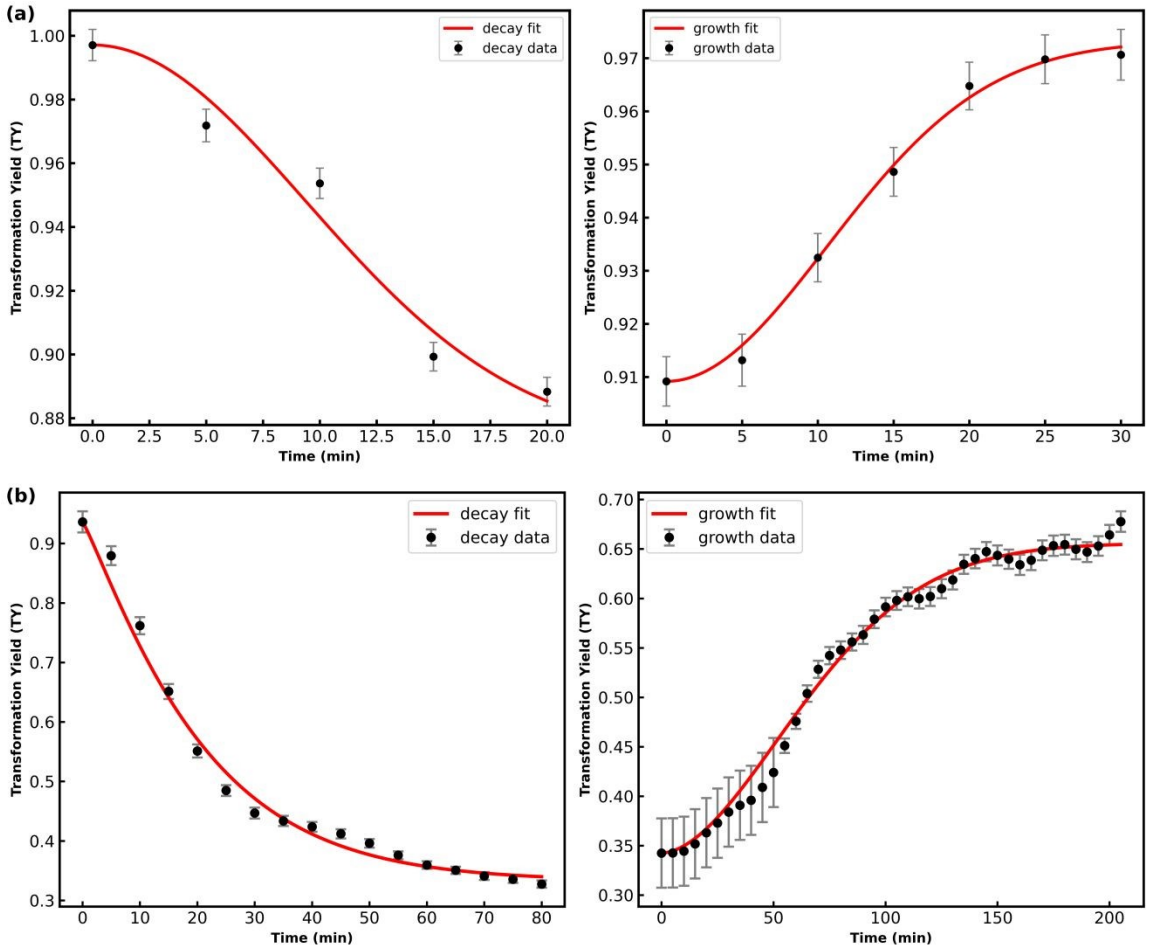

Figure 5. Transformation yield (TY) of silver acetate as a function of X-ray irradiation time at (a) ambient pressure (up to 60 min) and (b) 1.65 GPa (up to 300 min). Black circles represent experimental data. The decay region was fitted using a modified Avrami model (red solid line), while the growth region was fitted using the general Avrami equation (red solid line). Left panels show silver acetate decay behavior and the right panels show Ag growth behavior.

View Article Online
DOI: 10.1039/D5CP04790K

Figure 5 shows the transformation yield (TY) of silver acetate at ambient and 1.65GPa pressure as a function of X-ray irradiation time for 60 minutes and 300 minutes respectively. At 1.65 GPa, the transformation yield (TY) decreases to approximately 0.33 ± 0.02 after 80 minutes of irradiation. However, following this initial decline, TY exhibits a gradual upward trend. After 5 hours of irradiation, the transformation yield (TY) reaches 0.66 ± 0.03. The resulting structural and chemical changes are consistent with primary X-ray induced damage, arising from electronic relaxation processes initiated by X-ray photo absorption[10,45–50]. When a molecule or atom absorbs a high energy X-ray photon, a core electron is either excited to a higher level or ejected. This process triggers a series of relaxation steps[10,50,51]. The initiation and evolution of these relaxation pathways depend on the system's chemical composition and on the interatomic/intermolecular distances[52–55]. Consequently, X-ray irradiation perturbs electrons and can destabilize oxidation states. Depending on external conditions such as temperature and pressure, the system undergoes structural and chemical transformations. It is important to note that electronic relaxation occurs on a very small timescale, and its probability strongly depends on the number of absorbed X-ray photons[51,56]. Because of the X-ray flux in our experiment, the transformation of silver acetate at 1.65 GPa pressure proceeds slowly (on the order of 5 minutes to several hours). The difference in the final TY after 300 minutes of irradiation, together with the structural and chemical changes observed by X-ray-induced at high pressure, indicates that high pressure plays a key role in the rate of formation of silver. To evaluate how high pressure (HP) influences the transformation rate (TR) of X-ray-induced Ag formation, we applied the Avrami model in two stages: (i) the initial decrease in TY and (ii) the increase in TY. In the first stage upto about 20 minutes at ambient and 80

View Article Online
DOI: 10.1039/D5CP04790K

minutes at 1.65 GPa the silver acetate XRD peaks drop, whereas small silver peaks begin to appear although the overall growth of silver peaks are not clear (Figure 2). At 1.65 GPa pressure the TY decrease shown in Figure 5 likely reflects a reduction in electron density, indicating that decomposition of the compound is the dominant process in this initial region. In the later irradiation period (right plot), the slow growth of new XRD peak shows that the chemical and structural transformation of silver acetate into silver structure becomes the prevailing mechanism. In Figure 5, the decay and growth regions clearly illustrate the transition between the two regimes. The first plot (left) data is fitted with the modified Avrami equation (equation 2) to describe the silver acetate transformation rate, and the second plot (right) data is fitted with the general Avrami equation (equation 3) to describe the silver formation rate at ambient and 1.65 GPa.

The first region of Figure 5 corresponding to the modified Avrami equation

Equation (2) – Decay region:

$$TY(t) = 1 - TY_{\infty} * (1 - \exp\{-(k\,t)^{n}\}) \quad 2.$$

while in the second region, the standard Avrami growth expression was used:

Equation (3) – Growth region:

$$TY(t) = TY_{\infty} * (1 - \exp\{-(k\,t)^{n}\}) \quad 3.$$

Here, TY(t) is the transformation yield at time t, and TY_{∞} is the final TY at the end of the selected transformation region. The parameter k is the rate constant, t is specified time, and n is the Avrami exponent, which reflects the nucleation and growth geometry of the crystals[57]. The Avrami model was first developed to describe phase changes in solids at a constant temperature and later extended to studies of polymer crystallization. In this framework, the kinetics of crystal growth typically produce an increasing S-shaped

View Article Online
DOI: 10.1039/D5CP04790K

(sigmoidal) curve over time[58–60]. The original Avrami equation had shortcomings, particularly in reliably determining the rate constant. Khanna and Taylor extended the model by allowing k to be a function of the Avrami exponent n, leading to a more precise description of transformation kinetics[61]. Note that the Avrami model is intended for crystalline growth, where the progress typically shows an upward sigmoidal trend. Kinetics indicate mix of precursor decomposition (decay) and product formation (growth)[62]. To model the initial decrease of the transformation yield (TY), we applied the modified Avrami form given in Eq. (2). The resulting fits for the selected pressure conditions are shown in Figure 5, and the corresponding Avrami parameters extracted from these fits are listed in Table 2. Parameters obtained from fitting Eq. (3). for the general Avrami growth region are listed in Table 3.

Table 2. Modified Avrami parameters k, n, and TY∞ obtained from fitting the first region (decay).

Pressure (GPa)	k (h^{-1})	n	TY∞
Ambient	4.52 ± 0.01	1.86 ± 0.06	0.86 ± 0.01
1.65	2.81 ± 0.05	1.13 ± 0.08	0.33 ± 0.02

Table 3. Avrami parameters k, n, and TY∞ obtained from fitting the second region (growth).

Pressure (GPa)	k (h^{-1})	n	TY∞
Ambient	3.91 ± 0.01	1.90 ± 0.07	0.97 ± 0.01
1.65	0.73 ± 0.02	1.65 ± 0.08	0.66 ± 0.03

In the Avrami model, the transformation is considered to begin at time t = 0, when the molecular system remains in its initial structural phase[60,63]. In our experiment, the

View Article Online
DOI: 10.1039/D5CP04790K

XRD data shown in Figures 2 indicated that the formation of silver began after approximately 25 minutes of irradiation at ambient pressure and after about 25 minutes at 1.65 GPa. To apply the most appropriate Avrami description, we set $t = 0$ for both curves at their lowest observed TY values TY = 0.86 ± 0.01 at t = 20 minutes for ambient pressure and TY = 0.33 ± 0.02 at t = 80 minutes for 1.65 GPa indicate the minimum. We then fitted the corresponding decay and growth regions for the 1.65 GPa data. Table II indicates that the rate constant (k) is higher under ambient conditions, consistent with a faster decomposition of silver acetate. However, a higher k at ambient does not, means itself, yield clean metallic silver, additional parameters are required for selective silver formation. At 1.65 GPa, the decomposition proceeds are controlled with pressure and metallic silver forms under X-ray irradiation over time, at a slower overall pace. The values of n are comparable to those obtained for the first (decay) region, indicating that the transformation is diffusion controlled[62]. An Avrami exponent suggests that the mechanism and effective dimensionality of silver formation are similar to those of silver acetate decomposition. At 1.65 GPa pressure, the growth curve reaches almost plateau within 300 minutes of irradiation. This indicates that the formation of silver from the sample reached a maximum. The speed and effectiveness of electronic relaxation in the initial stage drives the X-ray induced damage and depends on interatomic and intermolecular distances[64–66] . Electronic relaxation pathways are also influenced by the local chemical environment and charge distribution. Consequently, X-ray induced photochemistry involves multiple coupled steps and can be more complex than the simplified description used here[67–69]. These observations suggest that higher pressure enhances the efficiency of

View Article Online
DOI: 10.1039/D5CP04790K

certain chemical and structural transformations, in line with the evolution of the XRD pattern observed at ambient and elevated pressures (Figure 1). As a function of time, higher pressures reduce molecular mobility, which can hinder the reorganization pathways needed for silver formation. This is consistent with our observations that metallic silver forms at ambient pressure and at 1.65 GPa, whereas no clear structural or chemical transformation is detected at 4.0 GPa (Figure 2). The X-ray diffraction pattern unambiguously shows of the decomposition of silver acetate to metallic silver under X-ray irradiation with time. The peaks corresponding to the metallic silver reflection (111) and (200) emerge after 80 minutes at a pressure of 1.65GPa (Figure 3). The integrated intensity of the Ag (111) and (200) reflection peaks are quantified across the transformation using the Avrami equation of growth which shows the characteristic of diffusion-controlled nucleation and growth.

To provide additional insight for Avrami kinetics (Figure 5) into the reaction progress, we estimated the evolution of the silver acetate conversion to metallic Ag as a function of time from the XRD patterns. The conversion was obtained from the strongest peak ratio of integrated peak areas of a representative silver acetate reflection (010) (2.3° – 3.0° at 2θ) and a representative Ag reflection (111) (11.0° – 12.7° at 2θ), using pseudo-Voigt peak fitting for pressure 1.65 GPa. The reported values provide a relative measure of phase evolution rather than an absolute phase fraction[70]. The uncertainty associated with each data point was estimated by propagating the peak-fitting covariance and is shown in Figure 6. The increase in the estimated Ag fraction is accompanied by a corresponding decrease in the silver acetate fraction, confirming progressive conversion of the precursor.

View Article Online
DOI: 10.1039/D5CP04790K

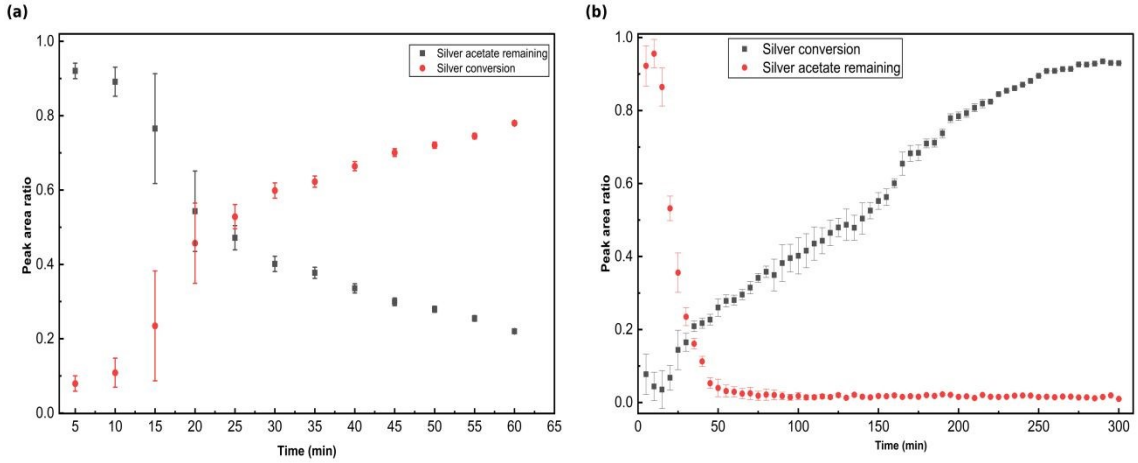

Figure 6. Time evolution of the conversion of silver acetate to metallic Ag estimated from relative XRD peak-area ratios. (a) Ambient-pressure data collected over 60 min. (b) Data collected at 1.65 GPa over 300 min.

We also calculated the Scherrer crystallite size to understand the formation of silver crystallites as a function of X-ray irradiation time at 1.65 GPa, using the Scherrer crystallite size equation.

$$D = \frac{K\,\lambda}{\beta\,\mathrm{Cos}\theta} \qquad 4.$$

Here, D is grain size in nm , K is the shape factor we usually use 0.94 for cubic shape[71,72] , β is the FWHM in radian and θ is the peak position in radian[73–75]. The full width at half maximum (FWHM) of the diffraction peaks was determined using a custom Python-based peak fitting routine. The Ag (111) reflection was selected for analysis due to its high intensity and minimal overlap with neighboring peaks. Each peak was fitted within a narrow 2θ window using a pseudo-Voigt function following linear background subtraction, yielding the measured peak width, $\beta_{\_mean}$, in 2θ units. Instrumental broadening was evaluated using a LaB_6 standard measured under identical experimental conditions,

View Article Online
DOI: 10.1039/D5CP04790K

including the same X-ray energy, detector geometry, and optical configuration. Multiple LaB_6 reflections were fitted using the same peak-fitting procedure, and the angular dependence of the instrumental peak width was modeled according to the Caglioti relation, in which the square of the instrumental FWHM is expressed as a function of diffraction angle through instrument-specific parameters obtained from least-squares fitting. The intrinsic sample broadening was then determined by subtracting the instrumental contribution from the measured peak width in quadrature. All FWHM values were converted to radians prior to correction, and the resulting instrument-corrected peak widths (FWHM) with including uncertainty were subsequently used for crystallite size analysis[76]. Prolonged hard X-ray irradiation under high pressure can generate lattice defects, including dislocations, stacking faults, and microstrain, leading to additional diffraction peak broadening. In this study, the progressive increase in the FWHM of the Ag (111) reflection indicates the development of microstructural disorder beyond crystallite size effects. Peak broadening may also be influenced by nonhydrostatic stress conditions within the diamond anvil cell, such as uniaxial compression and pressure gradients. Radiation damage can further contribute through defect formation and partial amorphization, occasionally accompanied by enhanced fluorescence. In some cases, partial peak narrowing over time suggests defect relaxation or annealing. Overall, the observed FWHM reflects a combined contribution from crystallite size evolution, strain, defect generation, and stress effects during irradiation and compression[77]. Microstrain is indeed an issue particularly with nonhydrostatic high pressure DAC experiments. The XRD patterns observed represent a statistical average of unit cell-based XRD. Thus, examining the XRD patterns of produced Ag, a combination of microstrain, bulk lattice damage (dislocations, faults, impurities etc.)

View Article Online
DOI: 10.1039/D5CP04790K

have a demonstrated effect. In this study, we have not sought to study the long-term changes in microstrain, pressure-induced broadening and bulk sample damage, and separation of product mixtures as it is challenging to separate these four contributing factors to broadening. The analysis focused on monitoring Ag formation using a single-reflection FWHM approach within the context of hard x-ray photochemistry. From the Scherrer crystallite size analysis of Ag, it was found that the crystallite size increased over the period of irradiation, indicating progressive growth of newly formed Ag nuclei. The plateauing of the crystallite size with extended X-ray exposure suggested that the sample had gradually converted to Ag crystallites, followed by the onset of crystallite size growth at 1.65 GPa. The Avrami growth behavior and the crystallite size evolution demonstrate that the X-ray assisted reduction of silver acetate proceeded through nucleation and growth of nanocrystalline metallic Ag, with both the kinetics and final domain size strongly influenced by the applied pressure. Based on the Avrami analysis, we evaluated the Scherrer crystallite size from the 80-minute growth point to 600 minutes and observed that the crystallite size increased progressively with time. The formation of metallic silver begins after approximately 80 minutes. Silver grains subsequently grow in size throughout continued irradiation, reaching a final size of 5.14 ± 0.02nm after 600 minutes, at which point the grain growth plateaus. These values were obtained by fitting the experimental data using a Boltzmann sigmoidal growth model, with a goodness of fit (R^2 = 0.985), confirming that crystallite growth occurred as a slow and controlled process under pressure during continuous X-ray irradiation.

View Article Online
DOI: 10.1039/D5CP04790K

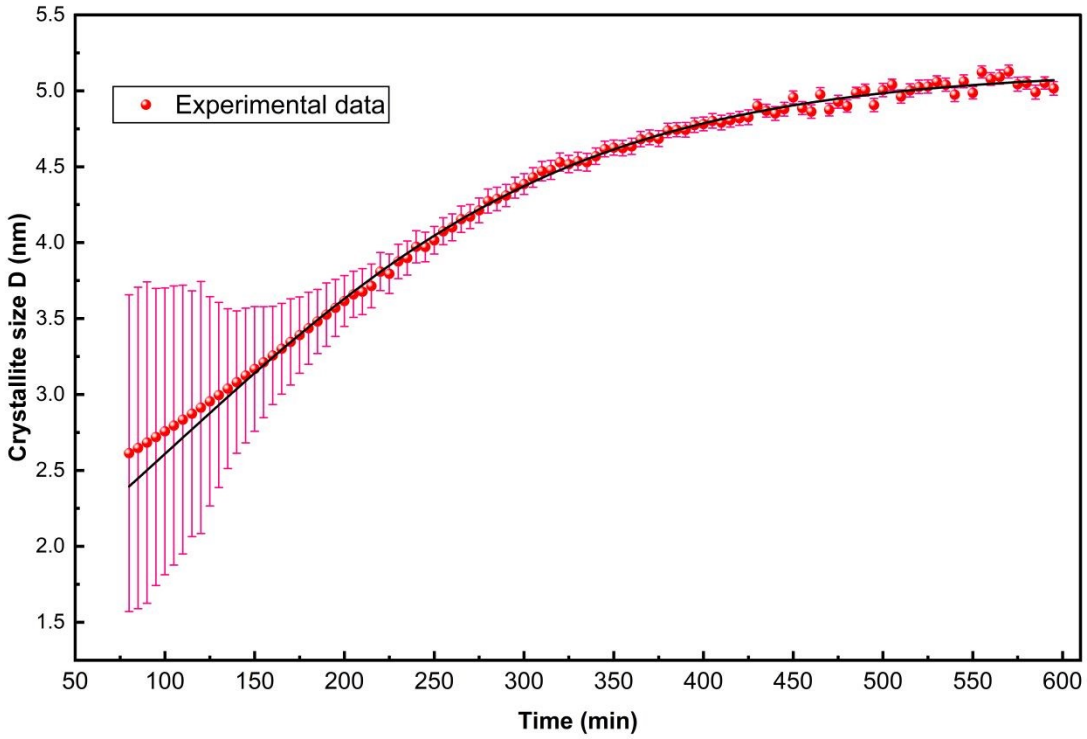

Figure 7: The size of crystallite in nm at pressure 1.65 GPa as a function of time. The red ball denotes the experimentally measured crystallite-size evolution during X-ray irradiation, and the black solid line corresponds to the Boltzmann sigmoidal fit.

Collectively, these results demonstrate that X-ray photochemistry provides an effective route for generating metallic silver from silver acetate, with pressure offering a practical means of tuning both the reaction yield and the characteristics of the final product.

4. Conclusions

In this paper, we have examined the role of x-ray irradiation of silver acetate. We have observed that silver acetate was reduced to silver metal under x-ray irradiation. With an aim of better understanding this x-ray induced metallization, the X-ray decomposition of

View Article Online
DOI: 10.1039/D5CP04790K

silver acetate was studied at different pressures to interrogate time-dependent decomposition and structural changes. The metallization reaction dramatically slowed with pressure, even appearing to cease at 4 GPa. At ambient pressure, the changes are gradual, whereas at 1.65 GPa the decomposition is clear and controlled as a function of time. The main product is metallic silver, consistent with a cubic (FCC) structure and with some amount of unreacted silver acetate remaining. These conclusions are supported by XRD, Avrami, relative measure of solid Ag evolution and crystallite size calculated data. At 4 GPa, we did not detect any metallic silver. Analysis with the Avrami model indicates that within 0–4 GPa, the rate and geometry of X-ray induced silver formation are independent of pressure whereas TY value was obtained. The formation of metallic silver begins after approximately 80 minutes of X-ray exposure. The FCC Ag grains subsequently grow in size throughout continued irradiation, reaching a final size of 5.14 ± 0.02nm after 600 minutes, at which point the grain growth plateaus. These values were obtained by fitting experimental data using a Boltzmann sigmoidal growth model. Our experiments show that X-rays could be matter interactions can be actively controlled by tuning experimental parameters, especially pressure. By compressing the sample, we adjust interatomic and intermolecular distances, which in turn modulates X-ray-induced photochemical pathways[6]. Using this pressure control, we demonstrate X-ray-induced synthesis of silver as a viable alternative route, with the potential to improve the synthesis of the nanoparticles in a controlled way. This study is important from the standpoint of better understanding mechanisms associated with x-ray induced metallization of salts which may find relevance in battery science and catalytic regeneration. Further work will endeavor to understand the

View Article Online
DOI: 10.1039/D5CP04790K

anion products and examine other salts that may be similarly reduced to constituent metals via *x-ray induced metallization*.

Credit authorship contribution statement

G. Bhandari analyzed the data and wrote the paper. M. Pravica conceived of and conducted the experiments and helped supervise data analysis. He also contributed to writing the paper. M. Kunz aided with the experiment and data analysis.

Declaration of competing interest

The authors declare no competing interests.

Data availability

Raw data were generated at the Advanced Light Source, Berkeley California]. Derived data supporting the findings of this study are available from the corresponding author (M.P.) on request.

Acknowledgments

We thank Petrika Cifligu for assistance with loading the samples into the diamond anvil cells. We gratefully acknowledge support from the U. S. Department of Energy, the Basic Energy Sciences (BES) program under Award Number DE-SC0023248. This research used resources of the Advanced Light Source, a U.S. DOE Office of Science User Facility under contract no. DE-AC02-05CH11231. Beamline 12.2.2 benefits from the support by SEES. SEE is supported by the National Science Foundation Division of Earth Science (EAR) SEES: Synchrotron Earth and Environmental Science (EAR – 2223273).

View Article Online
DOI: 10.1039/D5CP04790K

References

1 M. Pravica, E. Evlyukhin, P. Cifligu, B. Harris, J. Jae Koh, N. Chen and Y. Wang, *Chem. Phys. Lett.*, 2017, **686**, 183–188.
2 E. Evlyukhin, E. Kim, D. Goldberger, P. Cifligu, S. Schyck, P. F. Weck and M. Pravica, *Phys. Chem. Chem. Phys.*, 2018, **20**, 18949–18956.
3 M. Pravica, M. White and Y. Wang, *AIP Conf. Proc.*, 2017, **1793**, 060030.
4 T. Malik, P. Cifligu, M. Pravica, C. Park and E. Evlyukhin, *J. Phys. Chem. Solids*, 2025, **196**, 112351.
5 M. Pravica, L. Bai and N. Bhattacharya, *J. Appl. Crystallogr.*, 2012, **45**, 48–52.
6 E. Evlyukhin, P. Cifligu, M. Pravica, P. K. Bhowmik, E. Kim, D. Popov and C. Park, *Phys. Chem. Chem. Phys.*, 2023, **25**, 1799–1807.
7 T. Jahnke, *J. Phys. B: At., Mol. Opt. Phys.*, 2015, **48**, 082001.
8 A. F. Lua Sanchez, P. Cifligu, M. Graff, M. Pravica, P. K. Bhowmik, C. Park and E. Evlyukhin, *AIP Adv.*, 2023, **13**, 105031.
9 T. Jahnke, U. Hergenhahn, B. Winter, R. Dörner, U. Frühling, P. V. Demekhin, K. Gokhberg, L. S. Cederbaum, A. Ehresmann, A. Knie and A. Dreuw, *Chem. Rev.*, 2020, **120**, 11295–11369.
10 J. Zobeley, R. Santra and L. S. Cederbaum, *J. Chem. Phys.*, 2001, **115**, 5076–5088.
11 V. Stumpf, K. Gokhberg and L. S. Cederbaum, *Nat. Chem.*, 2016, **8**, 237–241.
12 F. Trinter, M. S. Schöffler, H.-K. Kim, F. P. Sturm, K. Cole, N. Neumann, A. Vredenborg, J. Williams, I. Bocharova and R. Guillemin, *Nature*, 2014, **505**, 664–666.
13 Z. Ni, Y. Chen, K. Shi and H. Zheng, *Ore Geol. Rev.*, 2025, 106450.
14 K. Wakamoto and T. Namazu, *Energies*, 2024, **17**, 4105.
15 A. Loiseau, V. Asila, G. Boitel-Aullen, M. Lam, M. Salmain and S. Boujday, *Biosensors*, 2019, **9**, 78.
16 S. Mukherjee, D. Chowdhury, R. Kotcherlakota, S. Patra, V. B, M. P. Bhadra, B. Sreedhar and C. R. Patra, *Theranostics*, 2014, **4**, 316–335.
17 M. R. Reithofer, A. Lakshmanan, A. T. K. Ping, J. M. Chin and C. A. E. Hauser, *Biomaterials*, 2014, **35**, 7535–7542.
18 X. Mao and G. Liu, *J. Biomed. Nanotechnol.*, 2008, **4**, 419–431.
19 D. Lin, S. Feng, H. Huang, W. Chen, H. Shi, N. Liu, L. Chen, W. Chen, Y. Yu and R. Chen, *J. Biomed. Nanotechnol.*, 2014, **10**, 478–484.
20 H. Hu, J. H. Xin, H. Hu, X. Wang, D. Miao and Y. Liu, *J. Mater. Chem. A*, 2015, **3**, 11157–11182.
21 J. Lai, W. Niu, R. Luque and G. Xu, *Nano Today*, 2015, **10**, 240–267.
22 G. A. Kelesidis and S. E. Pratsinis, *Chem. Eng. J.*, 2021, **421**, 129884.
23 C. J. Adams, M. A. Kurawa, M. Lusi and A. G. Orpen, *Cryst. Eng. Comm.*, 2008, **10**, 1790–1795.
24 R. Abbas, J. Luo, X. Qi, A. Naz, I. A. Khan, H. Liu, S. Yu and J. Wei, *Nanomaterials*, 2024, **14**, 1425.
25 N. P. U. Nguyen, N. T. Dang, L. Doan and T. T. H. Nguyen, *Processes*, 2023, **11**, 2617.
26 S. Iravani, H. Korbekandi, S. V. Mirmohammadi and B. Zolfaghari, *Res. Pharm. Sci.*, 2014, **9**, 385.
27 K. S. Siddiqi, A. Husen and R. A. K. Rao, *J. Nanobiotechnol.*, 2018, **16**, 14.

View Article Online
DOI: 10.1039/D5CP04790K

28 P. J. Jobst, O. Stenzel, M. Schürmann, N. Modsching, S. Yulin, S. Wilbrandt, D. Gäbler, N. Kaiser and A. Tünnermann, *Adv. Opt. Technol.*, 2014, **3**, 91–102.
29 J. Zhang, M. Ahmadi, G. Fargas, N. Perinka, J. Reguera, S. Lanceros-Méndez, L. Llanes and E. Jiménez-Piqué, *Metals*, 2022, **12**, 234.
30 M. Wang, Z. Zhang, G. Li and A. Jing, *Micromachines*, 2023, **14**, 617.
31 V. Marassi, L. Di Cristo, S. G. J. Smith, S. Ortelli, M. Blosi, A. L. Costa, P. Reschiglian, Y. Volkov and A. Prina-Mello, *R. Soc. open sci.*, 2018, **5**, 171113.
32 D. Bellet, M. Lagrange, T. Sannicolo, S. Aghazadehchors, V. H. Nguyen, D. P. Langley, D. Muñoz-Rojas, C. Jiménez, Y. Bréchet and N. D. Nguyen, *Materials*, 2017, **10**, 570.
33 M. Polívková, T. Hubáček, M. Staszek, V. Švorčík and J. Siegel, *Int. J. Mol. Sci.*, 2017, **18**, 419.
34 M. A. Saritala, M. Muzammil, M. R. Quddus, S. A. Razzak and M. M. Hossain, *Catalysts*, 2025, **15**, 560.
35 M. Nakano, T. Fujiwara and N. Koga, *J. Phys. Chem.*, 2016, **120**, 8841–8854.
36 D. Goldberger, C. Park, E. Evlyukhin, P. Cifligu and M. Pravica, *J. Phys. Chem. A*, 2018, **122**, 8722–8728.
37 High-pressure tools: ruby, https://millenia.cars.aps.anl.gov/gsecars/ruby/ruby.htm, (accessed January 24, 2026).
38 C. Prescher and V. B. Prakapenka, *High Press. Res.*, 2015, **35**, 223–230.
39 L. P. Olson, D. R. Whitcomb, M. Rajeswaran, T. N. Blanton and B. J. Stwertka, *Chem. Mater.*, 2006, **18**, 1667–1674.
40 B. H. Toby and R. B. Von Dreele, *J. Appl. Crystallogr.*, 2013, **46**, 544–549.
41 R. D. Deslattes, E. G. Kessler, P. Indelicato, L. De Billy, E. Lindroth and J. Anton, *Rev. Mod. Phys.*, 2003, **75**, 35–99.
42 J. Spreadborough and J. W. Christian, *J. Sci. Instrum.*, 1959, **36**, 116.
43 E. A. Owen and G. I. Williams, *J. Sci. Instrum.*, 1954, **31**, 49.
44 J. A. Kaduk, S. J. L. Billinge, R. E. Dinnebier, N. Henderson, I. Madsen, R. Černý, M. Leoni, L. Lutterotti, S. Thakral and D. Chateigner, *Nat. Rev. Methods Primers*, 2021, **1**, 77.
45 O. Marsalek, C. G. Elles, P. A. Pieniazek, E. Pluhařová, J. VandeVondele, S. E. Bradforth and P. Jungwirth, *J. Chem. Phys.*, 2014, **135**, 224510.
46 A. Hans, V. Stumpf, X. Holzapfel, F. Wiegandt, P. Schmidt, C. Ozga, P. Reiß, L. B. Ltaief, C. Küstner-Wetekam and T. Jahnke, *New J. Phys.*, 2018, **20**, 012001.
47 K. Gokhberg, P. Kolorenč, A. I. Kuleff and L. S. Cederbaum, *Nature*, 2014, **505**, 661–663.
48 F. Trinter, M. S. Schöffler, H.-K. Kim, F. P. Sturm, K. Cole, N. Neumann, A. Vredenborg, J. Williams, I. Bocharova and R. Guillemin, *Nature*, 2014, **505**, 664–666.
49 V. Stumpf, K. Gokhberg and L. S. Cederbaum, *Nat. Chem.*, 2016, **8**, 237–241.
50 O. Carugo and K. D. Carugo, *Trends Biochem. Sci.*, 2005, **30**, 213–219.
51 S. Yan, P. Zhang, V. Stumpf, K. Gokhberg, X. C. Zhang, S. Xu, B. Li, L. L. Shen, X. L. Zhu, W. T. Feng, S. F. Zhang, D. M. Zhao and X. Ma, *Phys. Rev. A*, 2018, **97**, 010701.
52 P. E. Barran, N. R. Walker and A. J. Stace, *J. Chem. Phys.*, 2000, **112**, 6173–6177.
53 O. Svoboda, D. Hollas, M. Ončák and P. Slavíček, *Phys. Chem. Chem. Phys.*, 2013, **15**, 11531–11542.

View Article Online
DOI: 10.1039/D5CP04790K

54 A. I. Kuleff, K. Gokhberg, S. Kopelke and L. S. Cederbaum, *Phys. Rev. Lett.*, 2010, **105**, 043004.
55 P. Zemenová, R. Král, M. Rodová, K. Nitsch and M. Nikl, *J. Therm. Anal. Calorim.*, 2020, **141**, 1091–1099.
56 J. N. Hay, *Brit. Poly. J.*, 1971, **3**, 74–82.
57 E. Evlyukhin, L. Museur, M. Traore, S. M. Nikitin, A. Zerr and A. Kanaev, *J. Phys. Chem. B*, 2015, **119**, 3577–3582.
58 M. Avrami, Granulation, *J. Chem. Phys.*, 1941, **9**, 177–184.
59 J. N. Hay and Z. J. Przekop, *J. Polym. Sci. Polym. Phys. Ed.*, 1978, **16**, 81–89.
60 Y. P. Khanna and T. J. Taylor, *Polym. Eng. Sci.*, 1988, **28**, 1042–1045.
61 C. G. Baek, M. Kim, O. H. Kwon, H. W. Choi and Y. S. Yang, *Cryst. Growth Des.*, 2017, **17**, 5684–5690.
62 T. Jahnke, A. Czasch, M. Schöffler, S. Schössler, M. Käsz, J. Titze, K. Kreidi, R. E. Grisenti, A. Staudte, O. Jagutzki, L. Ph. H. Schmidt, Th. Weber, H. Schmidt-Böcking, K. Ueda and R. Dörner, *Phys. Rev. Lett.*, 2007, **99**, 153401.
63 S. Marburger, O. Kugeler, U. Hergenhahn and T. Möller, *Phys. Rev. Lett.*, 2003, **90**, 203401.
64 G. Öhrwall, M. Tchaplyguine, M. Lundwall, R. Feifel, H. Bergersen, T. Rander, A. Lindblad, J. Schulz, S. Peredkov, S. Barth, S. Marburger, U. Hergenhahn, S. Svensson and O. Björneholm, *Phys. Rev. Lett.*, 2004, **93**, 173401.
65 Y. Ovcharenko, V. Lyamayev, R. Katzy, M. Devetta, A. LaForge, P. O'Keeffe, O. Plekan, P. Finetti, M. Di Fraia, M. Mudrich, M. Krikunova, P. Piseri, M. Coreno, N. B. Brauer, T. Mazza, S. Stranges, C. Grazioli, R. Richter, K. C. Prince, M. Drabbels, C. Callegari, F. Stienkemeier and T. Möller, *Phys. Rev. Lett.*, 2014, **112**, 073401.
66 K. Gokhberg and L. S. Cederbaum, *J. Phys. Conf. Ser.*, 2012, **388**, 062031.
67 C. Müller, A. B. Voitkiv, J. R. C. López-Urrutia and Z. Harman, *Phys. Rev. Lett.*, 2010, **104**, 233202.
68 K. Labisz and J. Konieczny, *Appl. Sci.*, 2024, **14**, 1702.
69 R. A. Matula, *J. Phys. Chem. Ref. Data*, 1979, **8**, 1147–1298.
70 G. I. Lampronti, A. A. L. Michalchuk, P. P. Mazzeo, A. M. Belenguer, J. K. M. Sanders, A. Bacchi and F. Emmerling, *Na.t Commun.*, 2021, **12**, 6134.
71 A. L. Patterson, *Phys. Rev.*, 1939, **56**, 978–982.
72 T. M. Gesing and L. Robben, *J. Appl. Crystallogr.*, 2024, **57**, 1466–1476.
73 Md. K. H. Shishir, M. Islam, Islam, M. Rahaman, H. Mustak, G. Mostafa and Md. A. Alam, *Results Surf. Interfaces*, 2025, **20**, 100595.
74 S. Ahmed, Md. K. H. Shishir, Md. T. Islam, Md. A. Rahaman, S. Aman, A. R. Aidid, S. I. Sadia, Md. M. Rana and Md. A. Alam, *Results Mater.*, 2025, **26**, 100673.
75 Md. A. Alam, Md. K. Hossain Shishir, D. Sarkar, R. K. Bishwas and S. A. Jahan, *J. Cryst. Growth*, 2025, **666**, 128230.
76 J. S. J. Hargreaves, *Catal. Struct. React.*, 2016, **2**, 33–37.
77 J. Wang, D. He and T. S. Duffy, *J. Appl. Phys.*, 2010, **108**, 063521.

View Article Online
DOI: 10.1039/D5CP04790K

Data Availability Statement

Raw data were generated at the Advanced Light Source, Berkeley California]. Derived data supporting the findings of this study are available from the corresponding author (M.P.) on request.